Supporting Information

Tailoring Defects in $SrTiO_3$ by One Step Nanoarchitectonics for Realizing Photocatalytic Nitrogen Fixation in Pure Water

Ashish Kumar,[a, d] Manisha Sharma,[a#] Sajjan Sheoran,[b#] Shilpi Jaiswal,[c#]

Abhijit Patra,[c*] Saswata Bhattacharya[b*] and Venkata Krishnan[a*]

[a]School of Chemical Sciences and Advanced Materials Research Center, Indian Institute of Technology Mandi, Kamand, Mandi 175075, Himachal Pradesh, India.

[b]Department of Physics, Indian Institute of Technology Delhi, New Delhi 110016, India.

[c]Department of Chemistry, Indian Institute of Science Education and Research Bhopal, Madhya Pradesh 462066, India.

[d]Department of Chemistry, Sardar Patel University Mandi, Mandi 175001, Himachal Pradesh, India.

*Corresponding authors: abhijit@iiserb.ac.in; saswata@physics.iitd.ac.in and vkn@iitmandi.ac.in

[#]These authors contributed equally to this work.

Materials Characterizations

The phase purity and structural properties of prepared samples was investigated by using powder x-ray diffraction (PXRD) recorded on a Rigaku Smart Lab 9 kW rotating anode diffractometer working in Bragg configuration with Ni-filtered Cu K_α irradiation (λ = 0.1542 nm) at 45 kV and 100 mA. The PXRD patterns were collected from a 2θ range of 20−80° with a scan rate of 2° per minute. Horiba LabRAM high resolution instrument was used for the Raman measurements with different lasers (532 nm, 633 nm and 785 nm). Morphology of the as prepared samples was investigated by using field emission scanning electron microscopy (SEM) FEI Nova Nano SEM-450 instrument. Transmission electron microscopy (TEM) and high resolution TEM (HRTEM) images were recorded on a Technai G 20 (FEI) S-twin microscope operating at 200 kV (accelerating voltage). The spatial distribution and presence of constituent elements in the prepared samples were studied by elemental mapping and EDAX spectroscopy facilities attached with the above mentioned TEM instrument. X-ray photoelectron spectroscopy (XPS) measurements were performed on a ThermoFisher Scientific NEXSA photoelectron spectrometer with Al K_α (1486.6 eV) dual anode as the source, operating at 12 kV anode voltage and 6.50 mA filament current. The XPS data were collected with a pass energy of 50 eV at 9 x 10^{-8} mbar vacuum and analysis of the obtained data was performed using Avantage software. Reflected electron energy loss spectroscopy (REELS) and ultraviolet photoelectron spectroscopy (UPS) measurements were carried to measure the band gap and valence band position of the materials, respectively. Etching experiments were also performed with the same XPS instruments. EPR spectra were recorded on Bruker EMX MicroX spectrometer. The optical absorbance and reflectance of the resultant samples were measured by diffuse reflectance spectroscopy (DRS) on a Perkin Elmer UV-visible-NIR Lambda 750 spectrophotometer using polytetrafluoroethylene (PTFE) polymer as standard. The Brunauer-Emmett-Teller (BET) surface area studies were carried out at 77 K on Quantachrome Autosorb-iQ-MP-XR system.

Theoretical Calculations

The spin-polarized calculations were performed using density functional theory (DFT) to understand the effect of oxygen vacancy in ST using Vienna *Ab Initio* Simulation Package (VASP) .[1] The electron-ion interactions are included using supplied projector augmented wave pseudopotentials.[2] We have used $3 \times 3 \times 2$ supercell consisting of 90 atoms to localize the oxygen-vacancy defect completely. Since the unit cell is cubic ($Pm\bar{3}m$ space group), only a single type of mono-vacancy of oxygen can be present .[3] In starting, we have relaxed structure with $3 \times 3 \times 3$ *k*-point Monkhorst-Pack[4] grid using Perdew-Burke-Ernzerhof (PBE)[5] generalized-gradient-approximation. In structural relaxation, the change in total energy between two ionic relaxation steps was set to be smaller than 0.01 meV and structures were relaxed till the Hellmann-Feynman force on each atom was smaller than 1 meV/Å. Cut-off energy of 550 eV was used throughout calculations. For a better description of excited states properties, the density of states (DOS) and single-point energy calculations are performed using $4 \times 4 \times 4$ *k*-point Monkhorst-Pack grid within the accurate nonlocal hybrid-functionals according to the Heyd-Scuseria-Erzenhof (HSE06) approach.[6] In HSE06 calculations, we have used an exact Fock parameter of 28% (Note that the 28% exact Fock parameter results in bandgap in agreement with the experimental observation instead of default 25%).

To understand the band edge positions, we have aligned the band edges of pristine ST with respect to the water redox potential levels. The CBM lies 0.80 eV above the water reduction potential, and VBM lies 1.18 eV below the water reduction potential. After that, we align the band edges of defected ST with respect to the pristine ST by observing the shift in the energy of CBM and VBM. We have calculated the fermi level shift by aligning the core states of Sr. The Fermi level in defected ST shifts upwards by 3.19 eV compared to the pristine ST.

Further, for N_2 fixation, the ST (001) surfaces with SrO- and TiO_2-Termination has been modeled as 2×2 supercell with a periodic 4-layer wherein the lower two layers are fixed and the upper two layers are optimized. We have inserted a vacuum of thickness 20 Å to avoid any interaction between periodic slabs. The $3 \times 3 \times 1$ *k*-grid has been used for single-point energy calculations of the surfaces. The Gibbs free energy of formation (ΔG) is for adsorption of hydrogen is calculated as follows:

$$\Delta G = E_{surf+H} - E_{surf} - \frac{E_{H_2}}{2} + \Delta E_{ZPE} - T\Delta S$$

Where E_{surf+H} and E_{surf} are the total energy of surfaces with and without hydrogen absorption, respectively. E_{H_2} is the total energy of a hydrogen molecule. ΔE_{ZPE} is the difference in zero-point energy between the adsorbed and the gas phase, T is the temperature and ΔS is the change in entropy. The vibrational energies determine the ΔE_{ZPE} and ΔS.

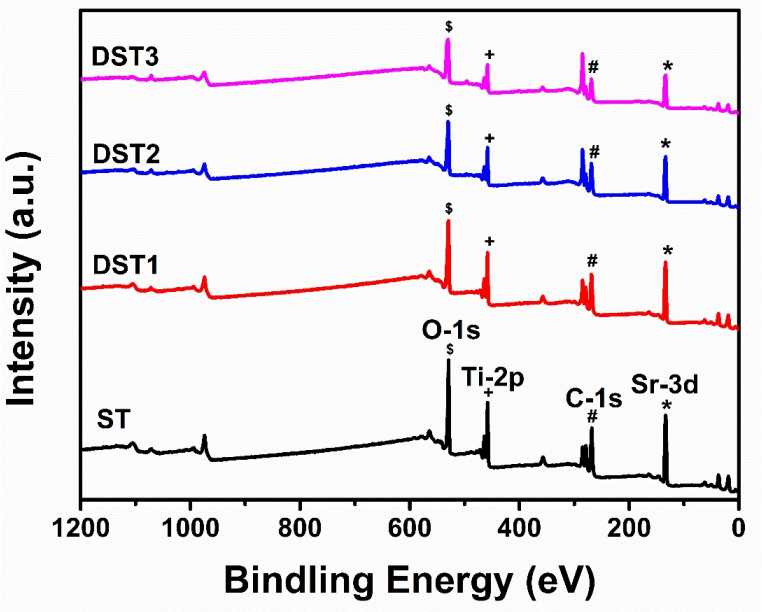

Fig. S1. XPS survey spectra of ST and DST materials.

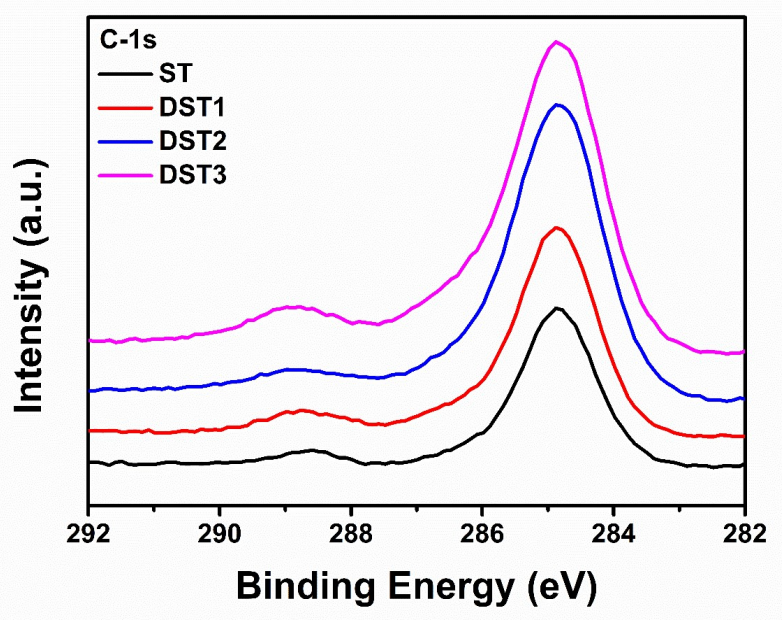

Fig. S2. High resolution C-1s XPS spectra of ST and DST materials showing the similar peaks for adventitious carbon in all samples.

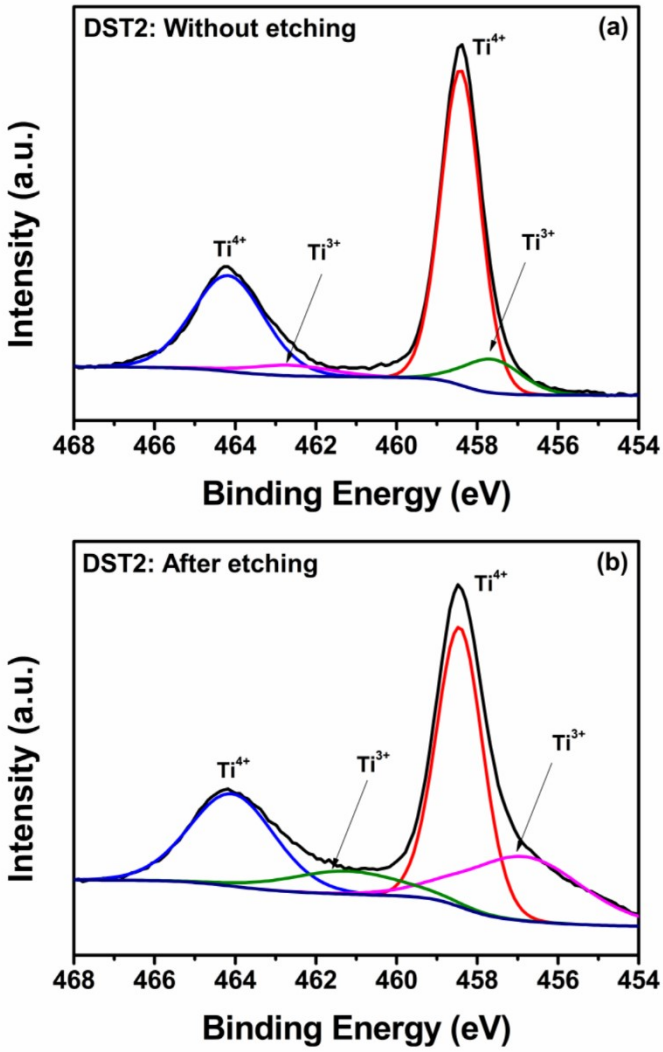

Fig. S3. High resolution XPS spectra of (a) DST2 without etching and (b) DST2 after etching (Etching parameters: Etching time = 2 minutes, 400 μm, Standard, CAE 50.0, 0.10 eV).

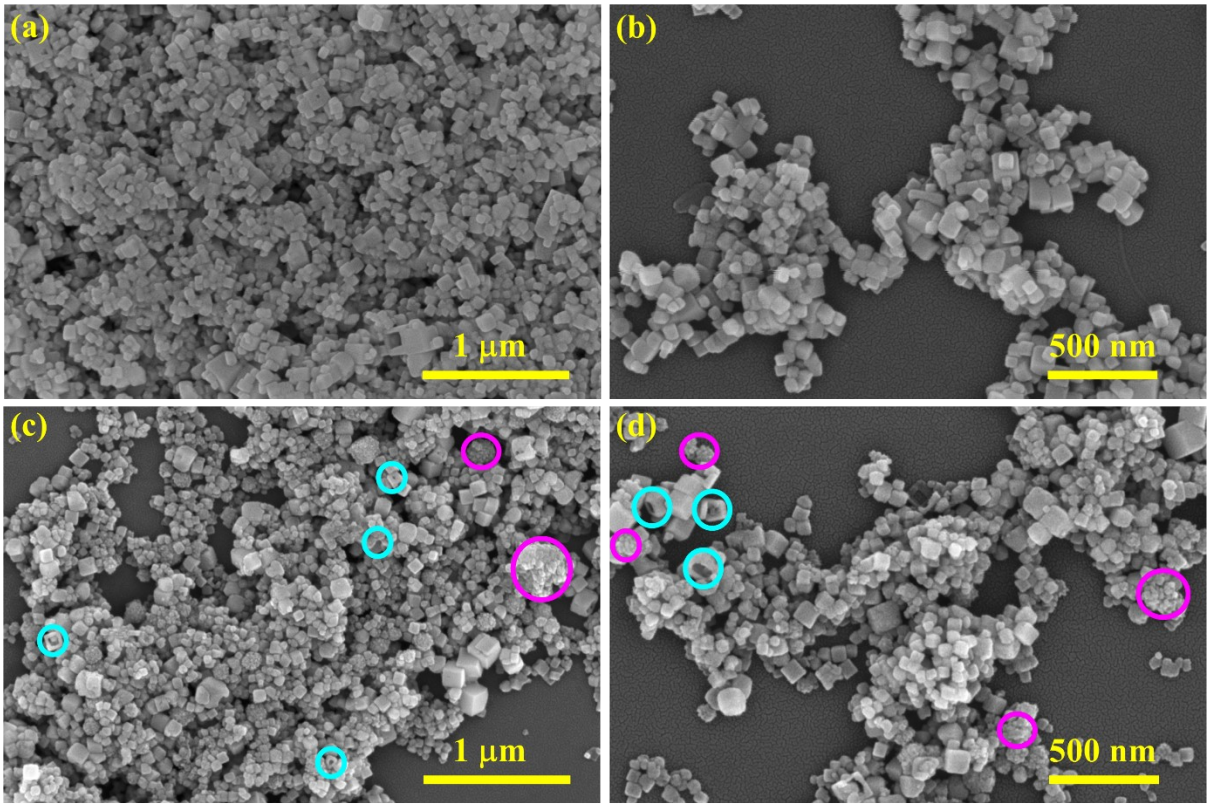

Fig. S4. SEM images of (a, b) ST showing nanocubes-like morphology and (c, d) DST2 showing nanocubes-like morphology along with hollow-nanocubes (encircled cyan) and small aggregates (encircled pink).

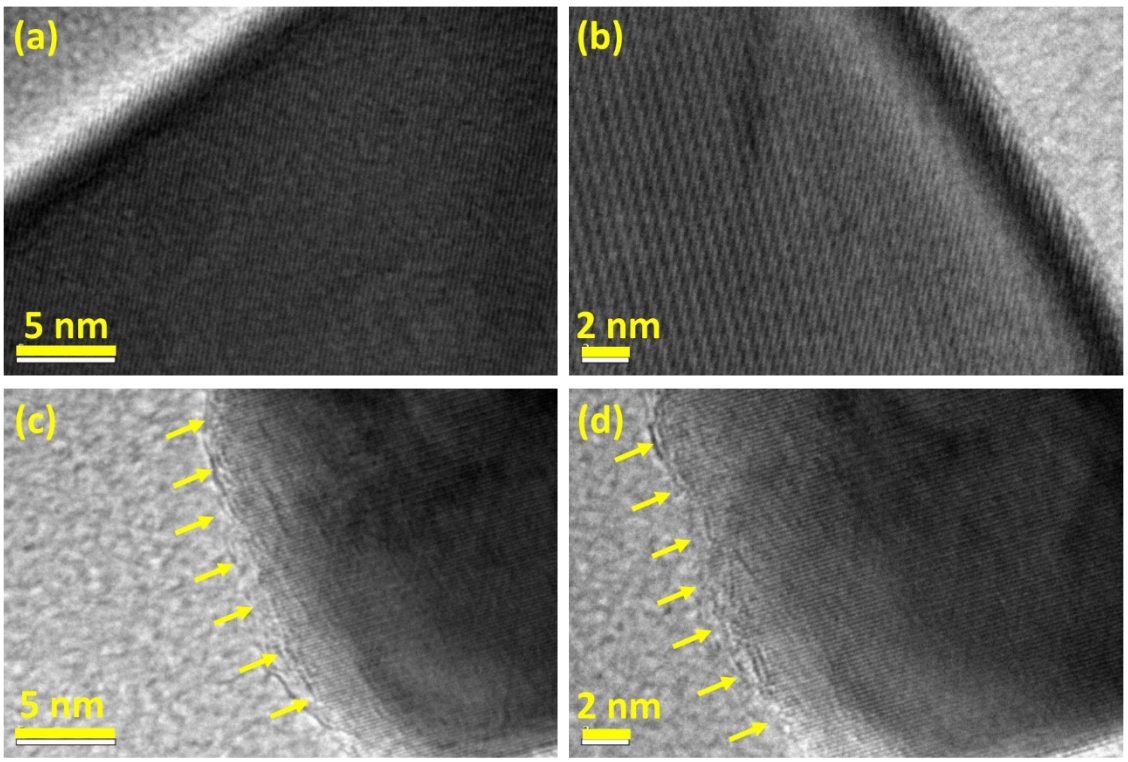

Fig. S5. HRTEM images of (a, b) ST and (c, d) DST2.

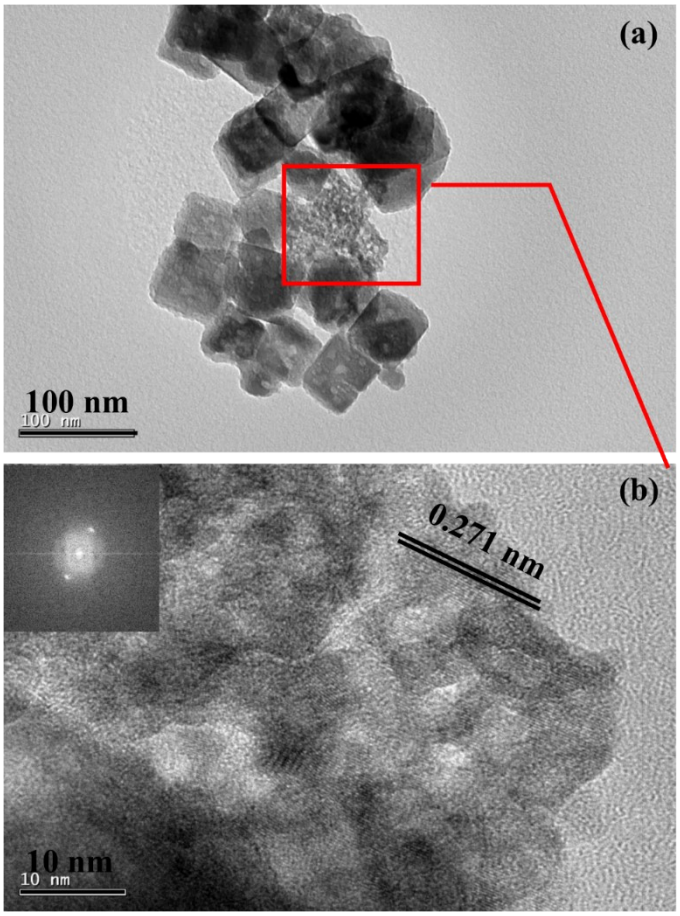

Fig. S6. (a) TEM image of ST showing porous aggregate like morphology and (b) HREM image of selected porous aggregate with FFT in the inset.

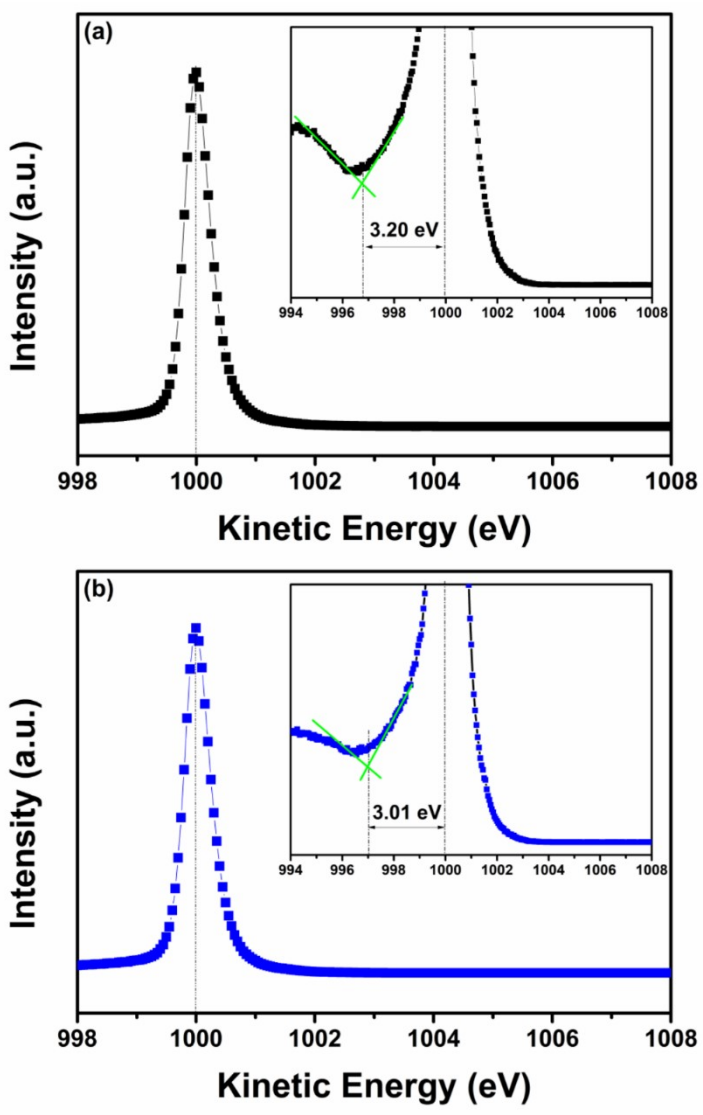

Fig. S7. REELS spectra of (a) ST and (b) DST2 materials.

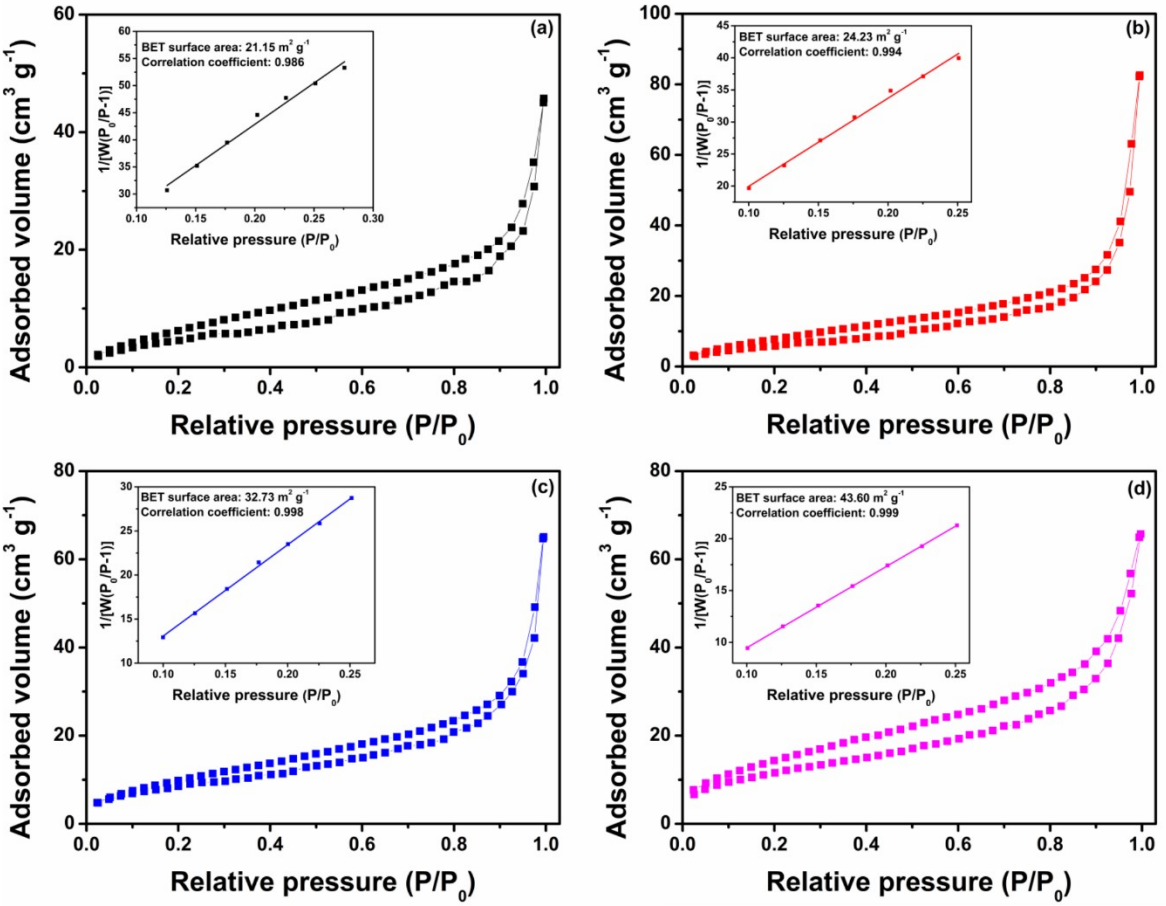

Fig. S8. BET adsorption-desorption isotherms of (a) pristine ST, (b) DST1, (c) DST2 and (d) DST3. BET surface area plots are presented in the inset.

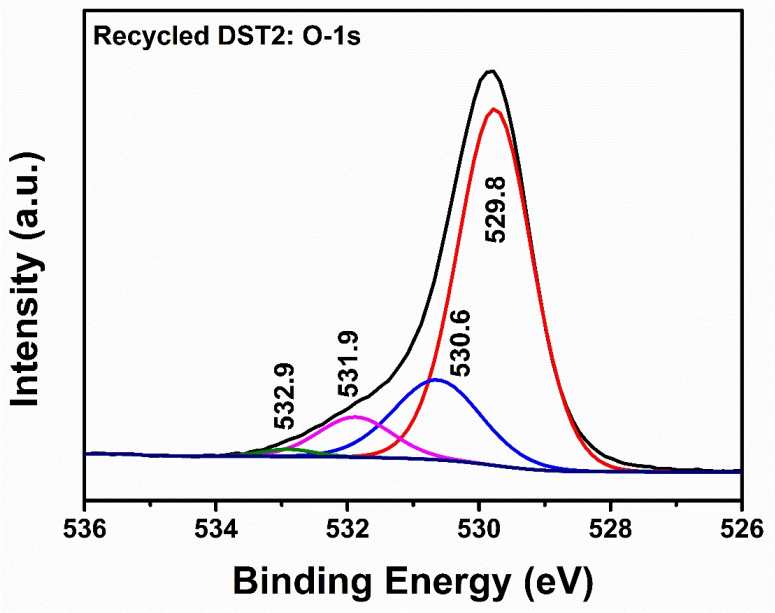

Fig. S9. High-resolution O-1s spectra of recycled DST2.

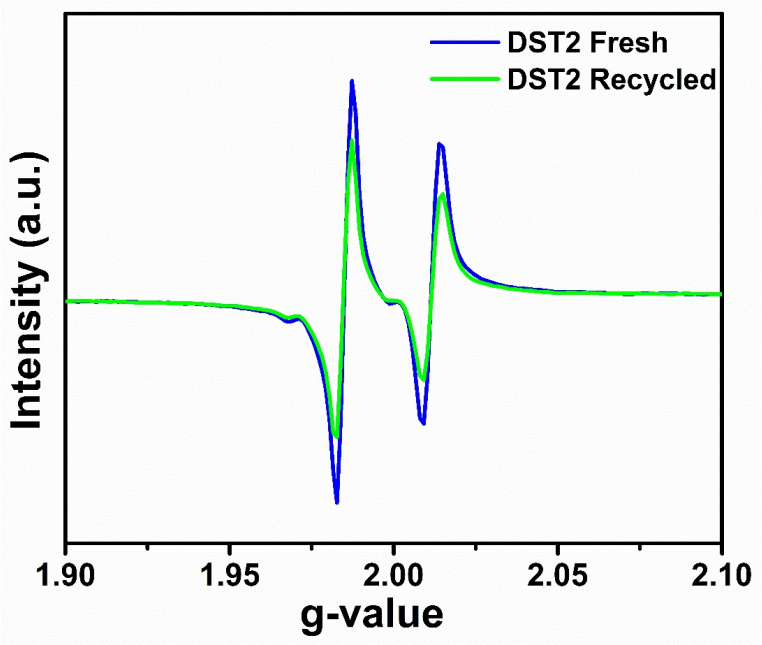

Fig. S10. Comparison of EPR spectra of fresh and recycled DST2.

Table S1. XPS elemental analysis for ST and DST materials.

Photocatalyst	Sr (At%)	Ti (At%)	O (At%)	N (At%)
ST	17.14	20.86	62.00	-
DST1	15.85	18.23	63.95	1.97
DST2	15.78	16.99	65.46	1.76
DST3	12.08	14.55	69.53	3.84

Table S2. Summary of photocatalytic NH_3 production in pure water under Ar and N_2 atmospheres for ST and DST catalysts.

Photocatalyst	**NH_3 produced under Ar atmosphere (μmol h^{-1})**	**NH_3 produced under N_2 atmosphere (μmol h^{-1})**	**Actual Amount of NH_3 produced (μmol h^{-1})**	**NH_3 produced in μmol h^{-1} g^{-1}**
ST	-	-	-	-
DST1	-	2.96	2.96	7.40
DST2	8.11	22.52	14.41	36.02
DST3	7.59	16.52	8.93	22.32

Table S3. Comparison of N_2 fixation performance of oxygen vacancy engineered $SrTiO_3$ with other similar materials.

Photocatalyst	**Synthesis procedure**	**Reaction medium**	**Light source**	**NH_3 generated (μmol g^{-1} h^{-1})**	**Ref.**
TiO_2 (Oxygen vacancies)	Annealing in presence of $NaBH_4$ under Ar atmosphere	10 vol% methanol in water	300 W Xe lamp Visible Light (> 420 nm)	324.86 2.21	[7]
Au/TiO_2 (Oxygen vacancies)	Solvothermal route followed by annealing under Ar atmosphere	10 vol% methanol in water	300 W Xe lamp (> 420 nm)	78.60	[8]
Cu-doped TiO_2 (Oxygen vacancies)	In Teflon-lined stainless steel autoclave	Pure water	300 W Xe lamp	78.9	[9]
InS_2 (Sulfur vacancies)	Solvothermal route followed by annealing under N_2 atmosphere	Pure water	300 W Xe lamp	52.49	[10]
Defect engineered $SrTiO_3$ (R-STO-3)	(Commercial $SrTiO_3$ + Li + ethylenedaimine) Reaction in glove box with 1-7 days stirring	Pure water	300 W Xe lamp	306.9	[11]
Defect engineered $SrTiO_3$ (MSTO-s)	Solvothermal route followed by annealing under H_2 and Ar atmosphere	10 vol% ethanol in water	300 W Xe lamp	109.2	[12]

Fe-doped $SrTiO_3$	Hydrothermal method followed by calcination	Pure water	300 W Xe lamp	30.1 μmol g^{-1} h^{-1}	[13]
Defect engineered $SrTiO_3$ (DST3)	One step Solvothermal method using Ascorbic acid as reducing agent	Pure water	Natural sunlight	36.0 μmol g^{-1} h^{-1}	This work

Step 1: Generation of monochloramine

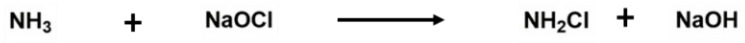

Ammonia Sodium Hypochlorite

Step 2: Nitroprusside-catalysed electrophilic substitution

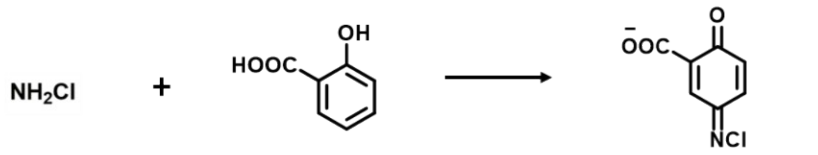

Monochloramine Salicylic acid Imine compound

Step 3: Oxidation-induced coupling reaction

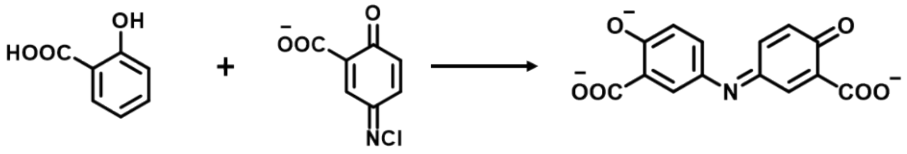

Salicylic acid Imine compound Indophenol

Product observed in Mass Spectroscopy

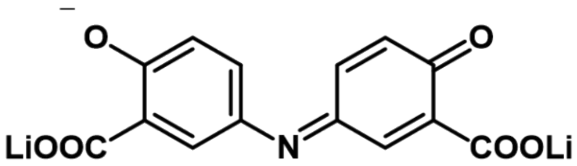

Exact Mass: 298.05
Observed Mass: 297.06 and 298.06

Fig. S11. The reactions involved in modified indophenol method and products observed in mass spectroscopy.

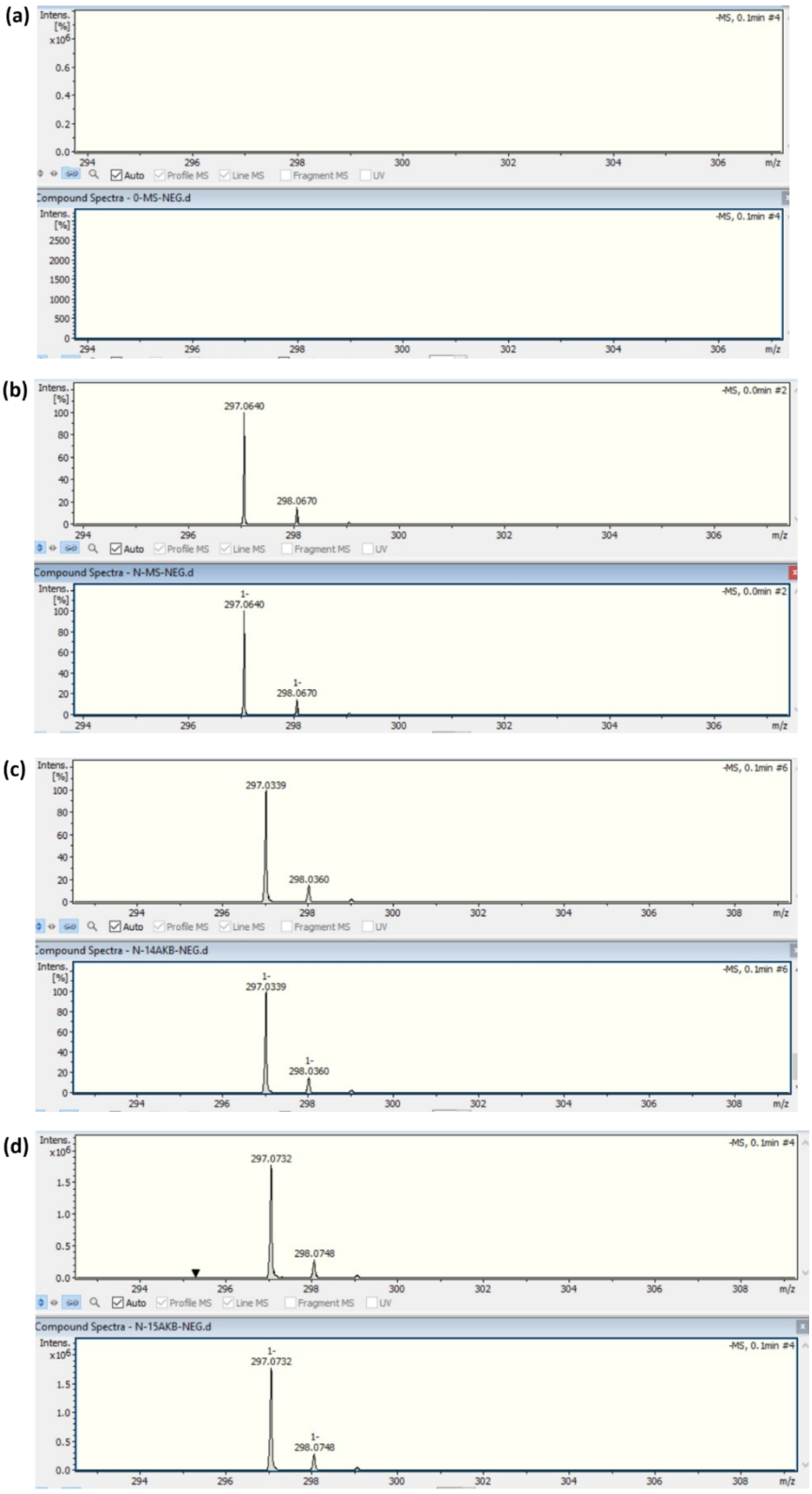

Fig. S12. Mass spectra of samples obtained by using modified indophenol method (a) pure water, (b) standard NH_3 solution, (c) reaction solution obtained after $^{14}N_2$ gas purging and (d) reaction solution obtained after isotope-labeled $^{15}N_2$ gas purging.

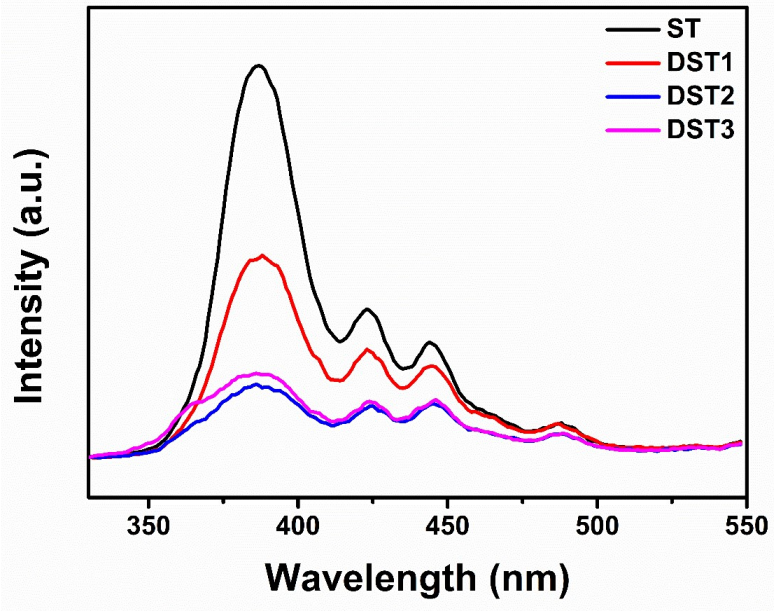

Fig. S13. PL spectra of ST and DST materials.

References

1. G. Kresse and J. Hafner, *Physical Review B*, 1993, **47**, 558.
2. G. Kresse and J. Hafner, *Journal of Physics: Condensed Matter*, 1994, **6**, 8245.
3. M. Kumar, P. Basera, S. Saini and S. Bhattacharya, *Scientific Reports*, 2020, **10**, 1-12.
4. H. J. Monkhorst and J. D. Pack, *Physical Review B*, 1976, **13**, 5188.
5. J. P. Perdew, K. Burke and M. Ernzerhof, *Physical Review Letters*, 1996, **77**, 3865.
6. J. Heyd, G. E. Scuseria and M. Ernzerhof, *The Journal of Chemical Physics*, 2003, **118**, 8207-8215.
7. G. Zhang, X. Yang, C. He, P. Zhang and H. Mi, *Journal of Materials Chemistry A*, 2020, **8**, 334-341.
8. J. Yang, Y. Guo, R. Jiang, F. Qin, H. Zhang, W. Lu, J. Wang and J. C. Yu, *Journal of the American Chemical Society*, 2018, **140**, 8497-8508.
9. Y. Zhao, Y. Zhao, R. Shi, B. Wang, G. I. Waterhouse, L. Z. Wu, C. H. Tung and T. Zhang, *Advanced Materials*, 2019, **31**, 1806482.
10. Z. He, Y. Wang, X. Dong, N. Zheng, H. Ma and X. Zhang, *RSC Advances*, 2019, **9**, 21646-21652.
11. J. Wang, T. Wang, Z. Zhao, R. Wang, C. Wang, F. Zhou, S. Li, L. Zhao and M. Feng, *Journal of Alloys and Compounds*, 2022, **902**, 163865.
12. B. Huang, Y. Liu, Q. Pang, X. Zhang, H. Wang and P. K. Shen, *Journal of Materials Chemistry A*, 2020, **8**, 22251-22256.
13. Z. Ying, S. Chen, T. Peng, R. Li and J. Zhang, *European Journal of Inorganic Chemistry*, 2019, **2019**, 2182-2192.